



# Machine learning models for prediction of electrochemical properties in supercapacitor electrodes using MXene and graphene nanoplatelets

Mohammed Shariq <sup>a,1</sup>, Sathish Marimuthu <sup>a,1</sup>, Amit Rai Dixit <sup>b</sup>, Somnath Chattopadhyaya <sup>b</sup>, Saravanan Pandiaraj <sup>c</sup>, Muthumareeswaran Muthuramamoorthy <sup>c</sup>, Abdullah N. Alodhyab <sup>c,d</sup>, Mohammad Khaja Nazeeruddin <sup>e,\*</sup>, Andrews Nirmala Grace <sup>a,\*</sup>

<sup>a</sup> Centre for Nanotechnology Research, Vellore Institute of Technology, Vellore 632014 Tamil Nadu, India

<sup>b</sup> Department of Mechanical Engineering, IIT(IISM) Dhanbad, Jharkhand 826004, India

<sup>c</sup> Biological and Environmental Sensing Research Unit, King Abdullah Institute for Nanotechnology, King Saud University, P.O. Box 2455, Riyadh, 11451, Saudi Arabia

<sup>d</sup> Department of Physics and Astronomy, College of Science, King Saud University, P. O. Box 2455, Riyadh 11451, Saudi Arabia

<sup>e</sup> Institute of Chemical Sciences and Engineering, École Polytechnique Fédérale de Lausanne (EPFL), Rue de l'Industrie 17, Sion CH-1951 Switzerland

## ARTICLE INFO

### Keywords:

Machine Learning  
Regression  
Artificial neural network  
MXene ( $Ti_3C_2T_x$ )  
Graphene nanoplatelets  
Supercapacitors

## ABSTRACT

Herein, machine learning (ML) models using multiple linear regression (MLR), support vector regression (SVR), random forest (RF) and artificial neural network (ANN) are developed and compared to predict the output features viz. specific capacitance ( $C_{sp}$ ), electrical conductivity ( $\sigma$ ) and sheet resistance ( $R_s$ ) for MXene/Graphene Nanoplatelets (GNPs) based energy storage devices. These output features are modeled as a function of wt% in different weight ratios of GNPs in MXene, optimum potential window and scan rates. The datasets are obtained by the real time output measurements through the experimental runs of these composites in different weight ratios. Among these models, ANN had achieved the highest performance followed by MLR, SVR and RF. From both the experimental and ANN results, the electrode with 20 wt% of GNPs in MXene (MG-80) exhibited the highest  $C_{sp}$  of 226.6F/g at 5 mV/s with a long cycle life having 84.2 % retention even after 5000 cycles of charging-discharging. ANN model is further utilized to predict the cyclic stability of MG-80 electrode upto 10,000 cycles and the results show the accuracy of the ML model to fabricate storage devices. Furthermore, the structure of MXene/GNPs composites are investigated by different characterization techniques. XRD spectra confirmed the successful synthesis of MXene and the successful intercalation of GNPs into MXene sheets. The morphology of the embedded GNPs in layered MXenes are determined through FE-SEM/EDX and HR-TEM analysis. The increase in the surface area and pore volume in the MXene/GNPs composite are revealed by BET measurements. XPS is utilized to find out the chemical element states of the bare MXene as well as its composite with GNPs.

## 1. Introduction

In recent days, rechargeable batteries are in growing demand for public transportation, EVs, electronic hardware devices such as laptops, touch pads, smartphones as well as in large scale commercialized energy storage devices. However, due to their functional and material limitations of low power densities, short cycle life, longer charging durations, poor thermal management and serious environmental concerns, it has compelled the researchers to look for substitutive energy storage technology such as supercapacitors (SCs). The demand for these SCs has

drastically increased with a view of its huge potential as alternative commercial energy storage systems [1–3]. In commercial SCs, activated carbon is widely employed as electrode material with different salts dissolved in organic solutions as electrolyte [4]. MXene, a new class of two-dimensional (2D) materials with a general configuration of  $M_{n+1}X_nT_x$ , (where M = transition metal, X = C and/or N, T<sub>x</sub> = attached surface termination and n = 1–4) showed the good prospects as an alternative electrode material with high areal charge storage capability [5–9]. It has large active surface area, high conductivity, high electron density and excellent hydrophilicity [10–13]. Additionally, MXene

\* Corresponding authors.

E-mail addresses: [mdkhaja.nazeeruddin@epfl.ch](mailto:mdkhaja.nazeeruddin@epfl.ch) (M. Khaja Nazeeruddin), [a nirmalagrace@vit.ac.in](mailto:a nirmalagrace@vit.ac.in), [a nirmalagladys@gmail.com](mailto:a nirmalagladys@gmail.com) (A.N. Grace).

<sup>1</sup> Authors equally contributed.

surface can be functionalized with  $=O$ ,  $-OH$ , and  $-F$  facilitating its stable dispersibility in de-ionized water and other organic solvents such as NMP, DMF, DMSO and ethanol [14]. However, recent works reported that by using bare MXene as an electrode material, the exfoliated layers are getting restacked due to the weak van der Waals forces and hydrogen bonding [15]. It restricts the ion transport between the active material and the electrolyte solution thereby hindering the active-sites accessibility as well as loss in the exposed surface area thus limiting the overall electrochemical performances [16–19]. Another challenge with MXene is its tendency to get easily oxidized at ambient conditions that significantly degrade the electrical conductivity ( $\sigma_e$ ) and shell life of MXene [20].

Therefore, designing the MXene based composites by embedding the nano-sized fillers of metal oxides [21], carbon materials such as CNTs, graphene structures [19,22] and conductive polymers [23] in-between the intercalated MXene layers could suppress the issue of coalescence and agglomeration and also increases the number of electroactive sites [24]. Graphene nanoplatelets (GNPs), also a 2D-layered carbon material comprising of multiple graphite planes and short stacks of layered sheets can be a promising matching candidate as a nano-filler for the intercalated MXene layers. It possesses large and accessible active surface area, superior electronic and mechanical properties such as strength and flexibility that can lead in achieving faster electron transport and rapid energy storage mechanism [25–27]. Therefore, GNPs integrated into MXene can effectively prevent the MXene layers from stacking and oxidation degradation, thus improving the overall chemical stability, mechanical flexibility and electrochemical activity [28,29].

Designing these composites with the optimized weight percent (wt. %) of MXene and GNPs for obtaining the maximum electrochemical and electrical performance with traditional experimental procedures consumes numerous resources, time and cause environmental degradation. Recently, machine learning (ML) based data driven models provided a critical tool that helps to understand and predict these characteristics with high precision and reliability without even performing a large number of experiments. These ML algorithms help in formulating complex models that define the relationships between the input and output features by utilizing the regression algorithms trained on the data collected from real experimentation. It helps in exploring the unknown spaces (i.e., the unexperimented data) by creating the datasets while demonstrating the utility of these models. These datasets comprise the input features (such as weight composition of the electrode material, potential window, electrode configuration, current density) and output features (specific capacitance ( $C_{sp}$ ), energy density, areal capacitance) for predicting the electrochemical behaviour of the fabricated supercapacitors. With the provided durable and consistent experimental data, the ML model gave precise and repeatable predictions for a large number of data points. The accuracy of these models is measured by using the performance metrics like root mean square error (RMSE), mean absolute error (MAE) and accuracy ( $R^2$ ) [30–32].

The following data-driven methods have been proposed for predicting the specific capacitance ( $C_{sp}$ ), sheet resistance ( $R_s$ ) and electrical conductivity ( $\sigma_e$ ) of the fabricated MXene/GNPs based supercapacitor electrodes: Multiple linear regression model (MLR), Support vector regression model (SVR), Random Forest (RF) and Artificial neural network model (ANN) respectively. These models will be trained for predicting the output features for different weight ratios of MXene/GNPs composites in accordance with the obtained experimental data. The following generated datasets will be compared with respect to the accuracy of these models and the model with the highest accuracy will be taken as the input for designing the ANN model. It will help us better to understand the correlation between the different input features such as wt.% of GNPs in MXene, working potential window, scan rates, electrode configuration on the output features.

In Zhou et al. [33], report, the following four models (generalized LR, SVM, RF and ANN) were developed and tested to study the correlation between the electrochemical performance specifically the  $C_{sp}$ ,

power density and heteroatomic doping of nitrogen and oxygen. The structural properties of the carbon materials, the chemical compositions of the electrode surfaces and the scan rate were the input parameters. Among these models, Artificial neural network (ANN) has given the best results with the highest  $R^2$  (0.85 – 0.97) and RMSE (0.32 to 31.5) values and was further used to evaluate the supercapacitor performance at in-operando conditions. The pyridinic and pyrrolic nitrogen doping resulted in achieving the maximum capacity to the higher micropore surface area. The ANN model also helped in determining the optimum micro and mesoporous surface area of  $1400\text{ m}^2/\text{g}$  and  $1000\text{ m}^2/\text{g}$  respectively in order to achieve the highest electrochemical performance of supercapacitors for N/O co-doped carbon electrodes ranging from low to high scan rates [33]. In another case study by Su et al., the ML models (LR, SVR, multilayer perceptron (MLP) and random tree (RT)) were developed to predict the electrical double layer capacitance of the carbon-based supercapacitors with seven input variables viz. potential window, the specific surface area, pore volume, pore size, ratio of  $I_D/I_G$ , N and O doping %. Based on the  $R^2$ , MAE and RMSE values, the performance of these models follows the ranks of  $RT > MLP > SVR > LR$  respectively. Out of the mentioned input variables, the specific surface area (30.1 %) and pore volume (24.1 %) are two important parameters affecting the EDLC performance while MLP model showed the best performance metrics with  $R^2$  value of 0.91 [34]. The data driven ML models such as RF, random subspace (RS), random committee (RC), multiclass classifier (MCC) and RT based regression algorithms were developed to predict the cyclic stability of the supercapacitors by creating large datasets of fifteen input parameters viz. electrode morphology, electrode composition, voltage window, applied current density, electrolytes, electrode configuration etc. The performance metrics of  $R^2$ , RMSE, MAE and Relative absolute error were calculated and compared to opt out the most predictive model. The principal component analysis method was further used to reduce the dimensionality of the dataset without sacrificing any statistical information. With respect to the grade and value prediction, the combination of (MCC + RF) and (RS + RC) respectively have performed significantly better than other models [35].

Wang et al. [36] using the ML method, the pseudo capacitance formulas of 200 MXenes in five types of materials including  $M_2X$ ,  $M_2X\text{-m}$ ,  $M_2XO_2\text{-m}$ ,  $M_2XS_2$  and  $M_2XS_2\text{-m}$ , were fitted based on their corresponding key features. The high pseudo capacitance distribution regions of the  $M_2X$  with and without surface groups were pointed out in the periodic table and the dominant factors of the pseudo capacitance of each type of material were revealed to clarify the physical origin of the high pseudo capacitance. This statistic result provides insights into the screening and design of two-dimensional MXenes pseudocapacitive electrode materials. Zhu et al. [37] have established a correlation between the capacitance of an Electric Double Layer Capacitor (EDLC) type supercapacitor with physical and chemical features of the carbon materials like pore volume, specific surface area, doping elements, etc. by using Artificial Neuron Network (ANN). Similarly, Su et al. [34] established the correlation between input features and supercapacitor performance by using Regression Trees (RT) and Multilayer Perception (MLP). Rahimi et al. [38] have predicted the specific capacitance of heteroatoms-rich Activated Carbon electrodes in EDLCs based on microstructural properties, Nitrogen/Oxygen functional groups, and operational parameters. The author has used MLR, SVR, RF and ANN for the prediction. Moreover Qian et.al gave a comprehensive overview of machine learning in the development of MXene materials for the applications of supercapacitor and batteries [39]. In other application of energy storage devices, ML models has been explored for the capacity estimation by building huge datasets from three different types of commercial Li-ion batteries. These datasets are used to build base models utilising ML techniques, such as the linear model (ElasticNet) and nonlinear models (XGBoost and SVR). The model construction using batteries that have positive electrodes was made of  $LiNi_{0.86}\text{Co}_{0.11}\text{Al}_{0.03}\text{O}_2$ . The other two datasets, which were utilised for

validation, were from batteries with positive electrodes made of  $\text{LiNi}_{0.83}\text{Co}_{0.11}\text{Mn}_{0.07}\text{O}_2$  and batteries with a mixture of  $\text{Li}(\text{NiCoMn})\text{O}_2$  and  $\text{Li}(\text{NiCoAl})\text{O}$  respectively. The XGBOOST is proven to be the best model achieving a RMSE value of 1.1 %. The transfer learning model for various battery systems adds a linear transformation before the basic model that helps to achieve high predictive performance within an RMSE of 1.7 %. In the system implementation of electric vehicle applications, the relaxation process of a battery after full charge can be readily achieved without the need for certain operating circumstances and voltage ranges, opening up a new potential for battery capacity estimation on utilising data-driven approaches [40]. The real-time electrochemical impedance spectroscopy (EIS) data and Gaussian process regression (GPR) based ML models were utilized to forecast the state of health and remaining useful life of Li-ion batteries. Interestingly, the model discovers the two prominent frequencies out of 120 possibilities in the range of 0.02 Hz-20 kHz, which are enough to estimate the capacity. EIS and GPR can be expanded to take into account more challenging and realistic settings, including changes in charge/discharge rate or fluctuations in cycle temperature over time [41].

The synthesis of Mxene/GNPs based composites involves complex multiple process of etching, washing and delamination. These intricate reaction steps makes it difficult to achieve the reproducibility and scalability. During the multiple synthesis protocols, impurities and contaminants in washing and delamination can pose a bigger challenge for achieving the high electrochemical performance. Optimizing the synthesis conditions to achieve the optimum interlayer spacing and intercalation of GNPs in MXene layers, consumes a high amount of resources. The synthesis methods involves expensive MAX phases and GNPs with energy intensive processes making the production of composites making the production process more economically as well as environmentally challenging. The ML algorithms can analyze the existing experimental data and identify the patterns in relationships between GNPs content in Mxene layers and the properties of Mxene/GNPs composites. These algorithms can help us to predict the optimal synthesis parameters for achieving the specific characteristics, reducing the need for extensive trial and error experimentation.

With all these relevant information, this study involves the development of four data driven models of supercapacitor-based electrodes using the obtained experimental results from different experimental iterations like varying the compositions of graphene (10–40 wt%) in MXene and investigating its influence on the electrochemical and electrical property indicators through ML models. The idea of evaluating the four developed ML models is to identify the model with the greatest predictive accuracy that could be used for predicting the optimum loading of active electrode materials for maximized electrochemical performance and good electrical properties. The introduction of GNPs into the exfoliated MXene layers were also investigated to know the increased interlayer spacing, improvement in the self-stacking issues and improved conductivity through XRD, FE-SEM and EDS analysis. These composites were further evaluated with cyclic voltammetry (CV) at high and low scan rates of 100 and 10 mV/s respectively, chronopotentiometry (CP) at a current density of 1 A/g, EIS and conductivity measurements. The obtained results from these compositions were used to create the datasets to train these models and predict the output features of the unperformed compositions of MXene/GNPs based composites. The developed model performances are evaluated and compared based on the performance metrics viz.  $R^2$  and RMSE values. Based on the experimental and computational results, a high  $C_{sp}$  of 226.6 F/g at a scan rate of 5 mV/s was achieved with the composite containing 20 wt% of GNPs content in MXene (MG-80). The best performing ML model was further utilized to predict the capacitive retention % of MG-80 upto 10,000 cycles.

## 2. Results and discussion

Developing an accurate and effective prediction model using MLR,

SVR, RF and ANN based regression algorithms for the best performing MXene and GNPs supercapacitor based on the optimum weight composition is essential to decrease the time required for designing and testing these electrodes. The datasets (as mentioned in Supporting Information in Section 1 as S1, S2, S3 and S4) were created with the performed experiments measuring the electrochemical performance and electrical properties of different loading of GNPs (10, 20, 30 and 40 % - named as MG-90, 80, 70, 60) to MXene. These datasets are randomly shuffled thrice and split into 80 % training data and 20 % testing data, which further ensures the performance of the ML models for validating the learned regression by preventing any bias during the training.

### 2.1. Generation of the dataset

Initially, the multilayered  $\text{Ti}_3\text{C}_2\text{Tx}$  MXene was synthesized by using the etchant composition of HCl, HF and DI water leading to the effective etching of Al layers from  $\text{Ti}_3\text{AlC}_2$  MAX phase and further swelled with LiCl as depicted in Fig. 1a. The XRD spectra of  $\text{Ti}_3\text{AlC}_2$  MAX phase,  $\text{Ti}_3\text{C}_2\text{Tx}$  MXene and its composition with GNPs at different wt.% are illustrated in Fig. 1b. The shift of the  $(002)_M$  peak of MXene from  $9.83^\circ$  to  $8.20^\circ$  indicates the removal of Al from the MAX phase [42]. A less intense peak around 60 degree indicates the presence of partially delaminated/swelled MXenes. The interlayer interactions in partially delaminated/swelled MXenes prevent restacking, ensuring a more consistent and controllable material for various applications [43,44]. Nevertheless, these MXenes that are partially delaminated or swelled may have restricted properties like rheological behaviour and conductivity when compared to their single layers; hence single-layer MXenes are preferred to enhance the electrochemical and electrical characteristics [45–47]. The d-spacing of swelled MXene increases from  $9.83 \text{ \AA}$  to  $10.78 \text{ \AA}$ . The bare GNPs exhibited a sharp peak at  $26.6^\circ$  of  $(002)_G$  signifying the typical hexagonal graphite lattice structure with ordered

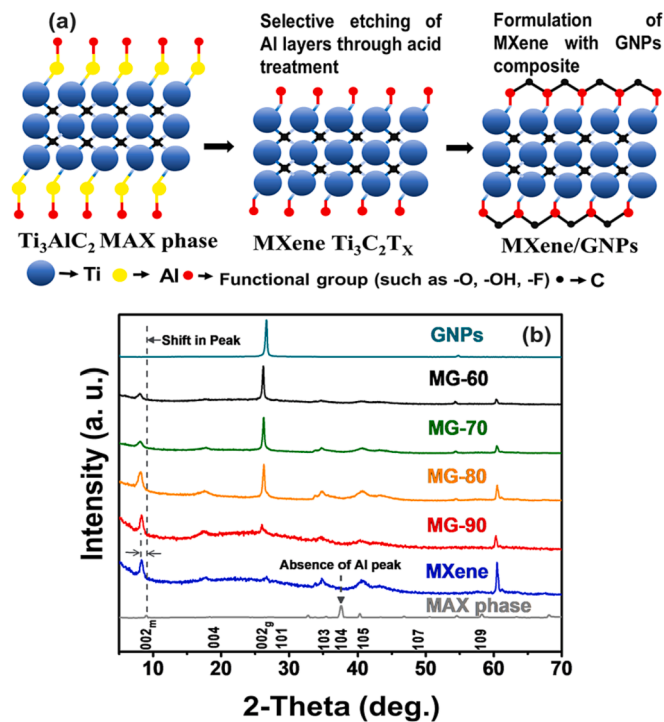


**Fig. 1.** Synthesis of MXene/GNPs composite. a) Schematic model of MXene etching from the MAX phase through mixed acid method and its interaction with GNPs. b) XRD spectra of the MAX, MXene and MXene/GNPs based composites. The shift of the  $002$  peak in (b) from the bare MXene to the MXene/GNPs based composites indicates the gradual increase of the d-spacing distance in between the MXene layers. This demonstrates the successful interlamellar insertion of GNPs into the MXene layers.

planes [28,49]. As the GNP content in the composite increases to 40 %, the corresponding characteristic peak of  $(002)_G$  becomes more and more prominent. Meanwhile, the  $(002)_M$  peak moderately shifts leftwards to  $8.0^\circ$  in MXene/GNPs composites and this shift in the peak implies the gradual increase of the d-spacing distance from  $10.78\text{ \AA}$  to  $11\text{ \AA}$  between the MXene layers, which suggests the successful interlamellar insertion of GNPs into MXene layers [28,50]. The intensity of  $(002)$  peak decreases with the increase of GNPs content, indicating a decrease in degree of stacking order of MXene layers due to hybridization with GNPs content [51]. It may result in the decrease of material density and electrical conductivity. This is also evident from the conductivity measurements as shown in Fig. 3f. Thus, the XRD spectra clearly demonstrate the interaction of GNPs with MXene sheets.

Fig. 2(a–c) displays the FE-SEM images of MXene, GNPs and MG-80 composite. The Fluoride based MILD etching of the MAX phase is performed to remove the Al layers. It results in the synthesis of accordion-like  $\text{Ti}_3\text{C}_2\text{Tx}$  MXene structures. Afterwards, the delamination process with  $\text{LiCl}$  resulted in the formation of swelled MXene layers with a layer size of about  $60\text{ nm}$  (Fig. 2a). These swelled MXene layered structures can be followed up by either vigorous shaking and stirring for 1 h to convert into few layered MXene [48,52]. These FE-SEM images of MXenes also confirm the 2D-layered structure without any visible

physical defects such as distorted boundaries and edges. In Fig. 2b, the GNPs comprises of short-sized stacked sheets of platelets shaped graphene. In the case of MG-80 composite, the FE-SEM images show the formation of composite structures with corrugated surfaces as observed in Fig. 2c–f. In addition, the elemental composition of the bare MXene and MG-80 composite was further investigated by obtaining the EDS spectra. Fig. 2g–h displays the wt.% with a standard deviation of the following Ti, C, F, Cl and O detected elements. MG-80 has shown an increase in the carbon composition in comparison with MXene, which further confirms the existence of GNPs in MG-80 composite.

HR-TEM was taken for MXene/GNPs (MG-80) composite that showed the stacking behavior as given in Fig. 3 [20,53]. HR-TEM image of MXene and MG-80 composite revealed that the GNPs were closely overlapped on the surface of the MXene sheets as shown in Fig. 3(a). Fig. 3(b) exhibits the TEM image of the pristine MXene. The interlayer spacing measurements (as mentioned in Supporting Information in Section 4, Fig S6) Fig. 3(c) reveal the lattice fringe of swelled / partially delaminated MXene with interlayer spacing of  $9.8\text{--}10.7\text{ \AA}$ , corresponding to the  $(002)$  crystal face of MXene (Fig. 3C1). In addition, the lattice fringe with the interlayer spacing of  $2.1\text{--}3.4\text{ \AA}$  can be assigned to the  $(002)$  crystal face of GNPs (Fig. 3C2). Notably, it can also be observed that GNPs interacted with MXene layers to generate a

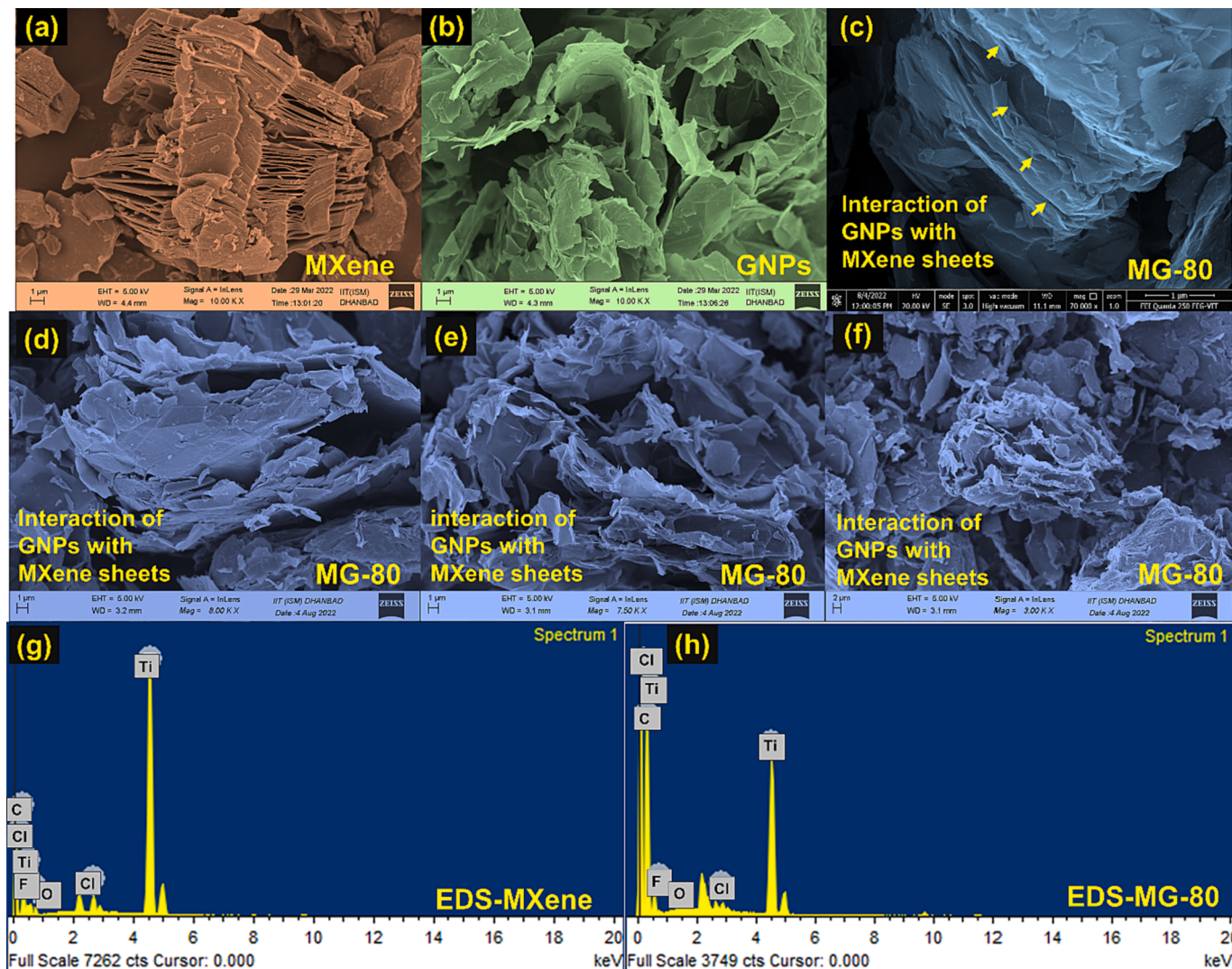


**Fig. 2.** Characterization of bare MXene, GNPs and its MG-80 composite. High resolution FE-SEM images of a) exfoliated MXene. b) GNPs. c-f) MG-80 composite. g) and h) are the EDS spectra of MXene and MG-80 respectively. The FE-SEM characterization shows the interaction of GNPs with MXene layers of MG-80 composite in (c-f) The EDS analysis for MXene and MG-80 composite in (g) and (h).

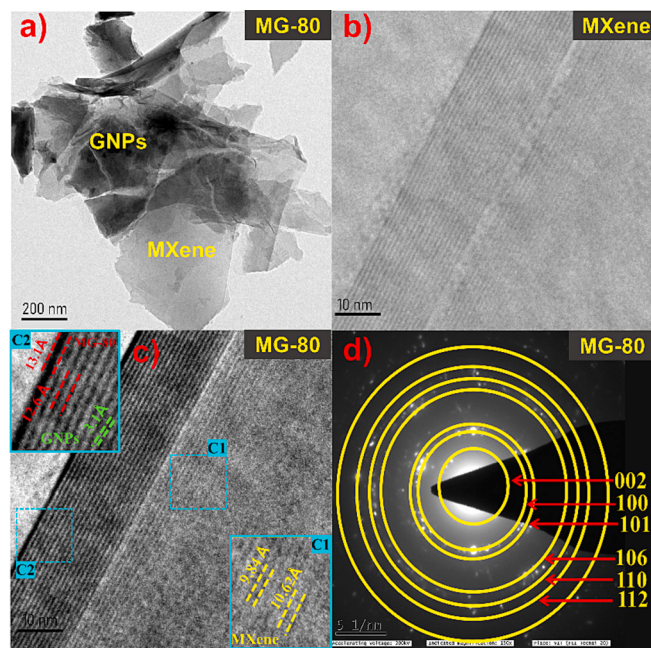


**Fig. 3.** HR-TEM characterization of MXene and MG-80 composite. a) MG-80 composite, b) pristine MXene, c) MG-80 composite revealing the interaction of GNPs with MXene, showing swelled MXene phase in the inset C1, MG-80 in the inset C2 d) SAED pattern of MG-80 composite.

sandwiched structure with the interlayer spacing of 11.4–13.1 Å (Fig. 3C2), much close to the total interlayer spacing of MXene and GNPs, demonstrating the heteroassembly of MXene and GNPs nanosheets on molecular scale [54]. This effectively prevents the face-to-face restacking of MXene and ensuring more electroactive sites exposed to electrolyte ions. The SAED pattern of MG-80 composite (Fig. 3d) is indexed using the Hough Diffraction analysis and contains the diffraction pattern from both the components of MXene and GNPs. The characteristic planes of graphene and the hexagonal pattern shows the presence of both the materials in the composite.

The electrochemical performance of the supercapacitor electrodes comprising of MXene and MXene/GNPs deposited on carbon electrode was evaluated by measuring the cyclic voltammetry (CV), galvanostatic charge–discharge (GCD), electrochemical impedance spectroscopy (EIS) and cyclic stability run. Initially, the CV tests for the bare MXene and MXene/GNPs composites viz. MG-90/80/70/60 electrodes were obtained at two different scan rates of 100 and 10 mV/s within a potential window of −0.1 to 0.35 V vs. Ag/AgCl as depicted in Fig. 4a and b. In comparison to the CV of different MXene/GNPs composites at a higher and lower scan rate and CP behaviour at 1 A/g (Fig. 4c), it was observed that an increase in the amount of GNPs content up to 20 wt% has effectively improved the electrochemical performance. On the other hand, the  $C_{sp}$  of these MXene/GNPs electrodes substantially decreased as the GNPs content increased to 30 wt% (MG-70) and 40 wt% (MG-60) respectively at the same scan rate. The EDLC behavior is observed during the CV measurements, ultimately, with the presence of redox behavior, the samples showed minimal pseudo capacitance also apart from its double layer capacitance [55]. The charge–discharge analysis in Fig. 4c revealed the symmetric triangular nature of the MXene/GNPs composites. As the GNPs in MXene increased from 0 to 20 wt%, these curves demonstrated the longer charge discharge times indicating the higher  $C_{sp}$  values. Furthermore, it decreases as the GNPs content further increased up to 40 wt%, which are in consistent with the CV results. The MG-80 composite has demonstrated an excellent and maximum charge–discharge time behaviour at a current density of 1 A/g as compared to all other compositions. The highest measured  $C_{sp}$  of 144.4F/g @ 10 mV/s (Fig. 4d) was achieved in MG-80 composite electrode, indicating

that the 20 wt% of GNPs as fillers (MG-80) in the MXene nanosheets is the most optimum amount that enhances the electrochemical performance of the electrode. With an initial addition of graphene to MXene, there is an increase in the capacitance that might be due to the less restacking than pure MXene. Thus, the MG-80 composite sample has achieved excellent conductivity and sufficiently large active surface area with optimum GNPs content as fillers in between the MXene layers. The synergistic effect and the large surface area with decreased restacking of MXene layers attributes to the fast diffusion and rapid ionic transportation enhancing the overall electrochemical storage capability of the composite. This interaction between the two materials has helped in achieving the highest conductivity due to the synergistic interactions between them. These GNPs fillers occupy the active sites in the MXene sheets. In the EIS measurements as shown in Fig. 4e, the depressed semi circled arc at a high frequency range was observed for all the samples, indicating that the ion transfer mechanism is kinetically controlled. Additionally, a straight line inclined 45° to the Z' axis is found in the low-frequency area indicating the diffusion-controlled process. Together, these two qualities form the electrochemical reactions for the supercapacitor electrodes in an acidic electrolytic medium [56]. In order to further understand the influence of different weight of GNPs in the MXene structures, the Nyquist plots of the MX-G composites are systematically tested and analysed. These data are used to accurately describe the resistance values of the MX-G samples and fit their impedance spectra as shown in Table 1. The extracted data reveal that the MG-80 has the lowest internal resistance which results in lower  $R_{series}$  and  $R_{CT}$  as compared to other composites. The values of  $R_{series}$  follows the order of MXene > MG-90 > MG-60 > MG-70 > MG-80 while  $R_{CT}$  follows the order of MG-60 > MXene and MG-70 > MG-90 > MG-80. The mean  $R_s$  and the  $\sigma_c$  for MXene, MG-90, MG-80, MG-70, MG-60 are  $126.6 \pm 6.1$ ,  $94.5 \pm 5.8$ ,  $69.8 \pm 4.3$ ,  $87.1 \pm 7.2$  and  $92.9 \pm 7.5 \Omega/\text{sq}$  and  $5158$ ,  $6800$ ,  $10214$ ,  $8900$  and  $7700 \text{ S/cm}$  respectively (Fig. 4f). These values correspond to the similar trend obtained with CV and GCD results.

When they are formed as a composite material, the compositions of the materials determine the overall properties. For instance, the overall capacitance largely depends on the intrinsic capacitance of the individual materials in the composite and also on the specific surface area of the material. These factors depend on the type of interaction between these two materials, which in turn depends on the composition of the loaded materials. Also, the surface area capacity of MXene and graphene are increased while preventing restacking through their combination. It is well known that MXene possesses large intrinsic capacitance due to its pseudocapacitive behavior whereas GNP possesses a lesser intrinsic capacitance and hence an increase in the mass fraction of GNP in the composite decreases the overall gravimetric capacitance. In MXene, the surface terminal groups in contact with the electrolyte influences the intrinsic capacitance and pseudocapacitance behavior of MXene via the interaction of the functional groups thus giving a higher capacitance value than graphene [56]. Thus, with an increased amount of graphene, the overall capacitance decreases and resistance increases. At the beginning, an increase in capacitance and a decreased resistance was observed for MG-80 and this might be due to the decreased restacking of MXene as compared to Pure MXene. Initial capacitance increase of up to 20 % GNP is thus due to the decreased restacking of MXene and hence more capacitance contribution of MXene in the composite as compared to pure MXene with higher restacking, leading to fast diffusion and rapid ionic transportation thereby improving the overall electrochemical storage capability of the composite.

## 2.2. Machine learning models performance

The obtained experimental results of the tested MXene/GNPs composites were given as inputs to the various proposed ML models and the results are discussed below. The reverse analysis of the experimental results to various ML models will predict the accuracy of each model and

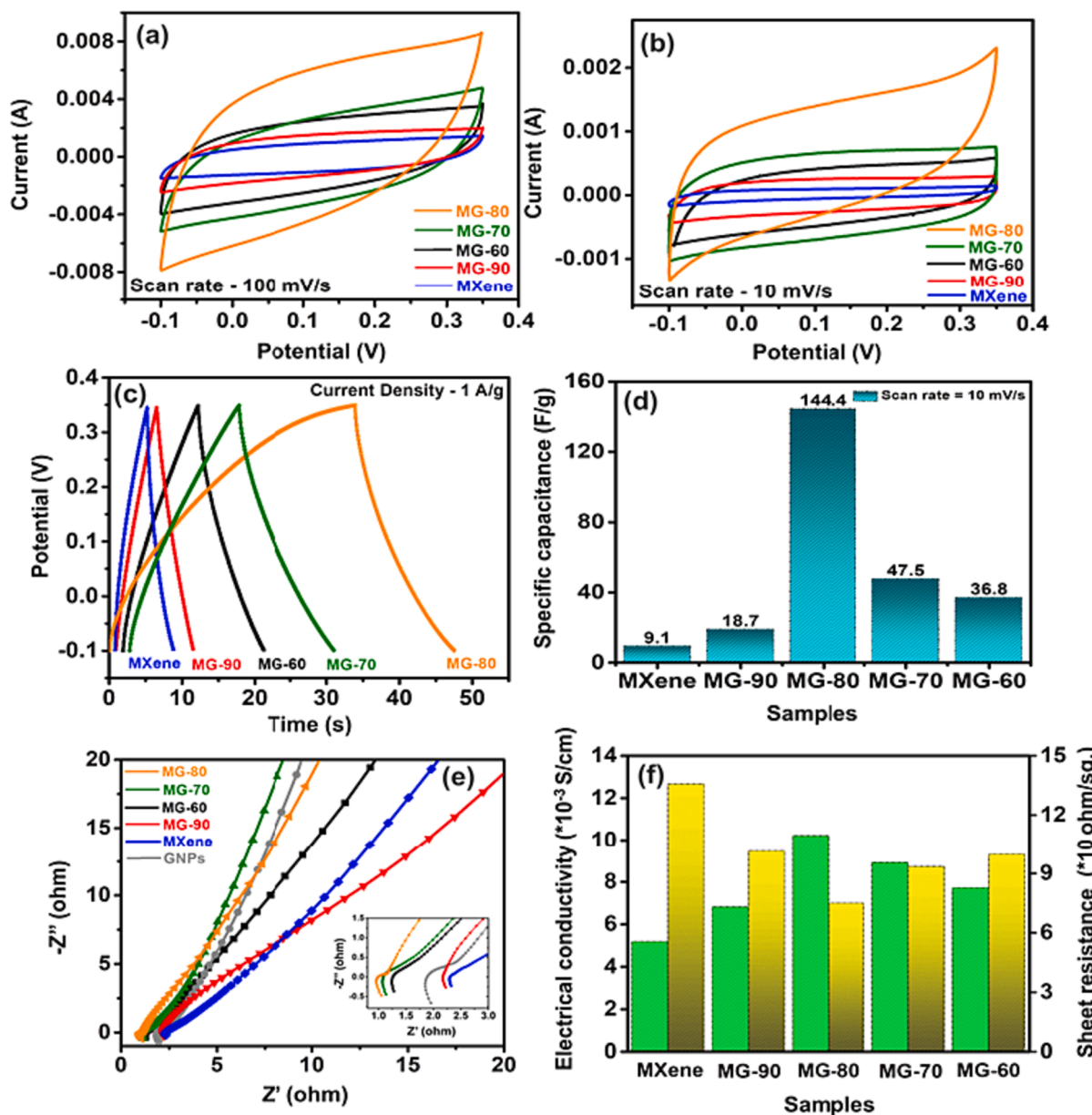


**Fig. 4.** Electrochemical measurements of MXene and MXene/GNPs composite electrodes in 1 M H<sub>2</sub>SO<sub>4</sub>. a) CV curves at a higher scan rate of 100 mV/s. b) lower scan rate of 10 mV/s. c) CP curves at a current density of 1 A/g. d) C<sub>sp</sub> values calculated at 10 mV/s. e) Electrochemical Impedance spectroscopy curves and f σ<sub>c</sub> and R<sub>s</sub> measured values. The CV and GCD tests in (a), (b) and (c) shows that by increasing the amount of GNPs content up to 20 wt% in MXene have effectively improved the electrochemical performance. Further increasing the GNPs content to 30–40 wt% the electrochemical performance decreases (d). The straight line inclined 45° to the Z' - axis in the low frequency area indicates the diffusion-controlled process for all the samples. The inset of (e) exhibit a depressed semicircle arc at high frequency range implies the kinetically controlled ion transfer mechanism. (f) Electrical conductivity and 4f of MXene and MXene/GNPs composite (MG-90, MG-80, MG-70 and MG-60).

**Table 1**  
Electrochemical impedance spectroscopy parameters of MXene and MXene/GNPs composites.

Sample Name	R <sub>series</sub> (in Ω)	R <sub>CT</sub> (in Ω)
MXene	2.32	0.29
MG-90	2.26	0.18
MG-80	1.07	0.11
MG-70	1.14	0.29
MG-60	1.28	0.42

that can be used as a preliminary tool to design future experimental engineering in designing supercapacitor electrodes.

Multiple linear regression model - MLR achieves the R<sup>2</sup> values

ranging from 0.78 to 0.81 for C<sub>sp</sub>, 0.87 to 0.90 for R<sub>s</sub>, 0.89 to 0.94 for σ<sub>c</sub>, which is significantly greater than that of SVR and RF models indicating its high accuracy as shown in Fig. 5a. RMSE values in the range of 10.14 to 11.9 for C<sub>sp</sub>, 9.07 to 10.4 for R<sub>s</sub>, 5.84 to 7.03 for σ<sub>c</sub> (Fig. 5b). These RMSE value ranges are lower than that of SVR and RF models signifying the less deviation of the output predicted features from the actual experimental values.

Support vector regression model (SVR) - As SVR is compared with MLR, generally SVR provides better performance as its computational complexity does not depend on the dimensionality of the input space. But, here MLR has performed better with the accuracy metrics due to the limited amount of the input features in the dataset. The R<sup>2</sup> value of SVR ranges from 0.65 to 0.72 for C<sub>sp</sub>, 0.79 to 0.82 for σ<sub>c</sub>, 0.79 to 0.85 for R<sub>s</sub>,

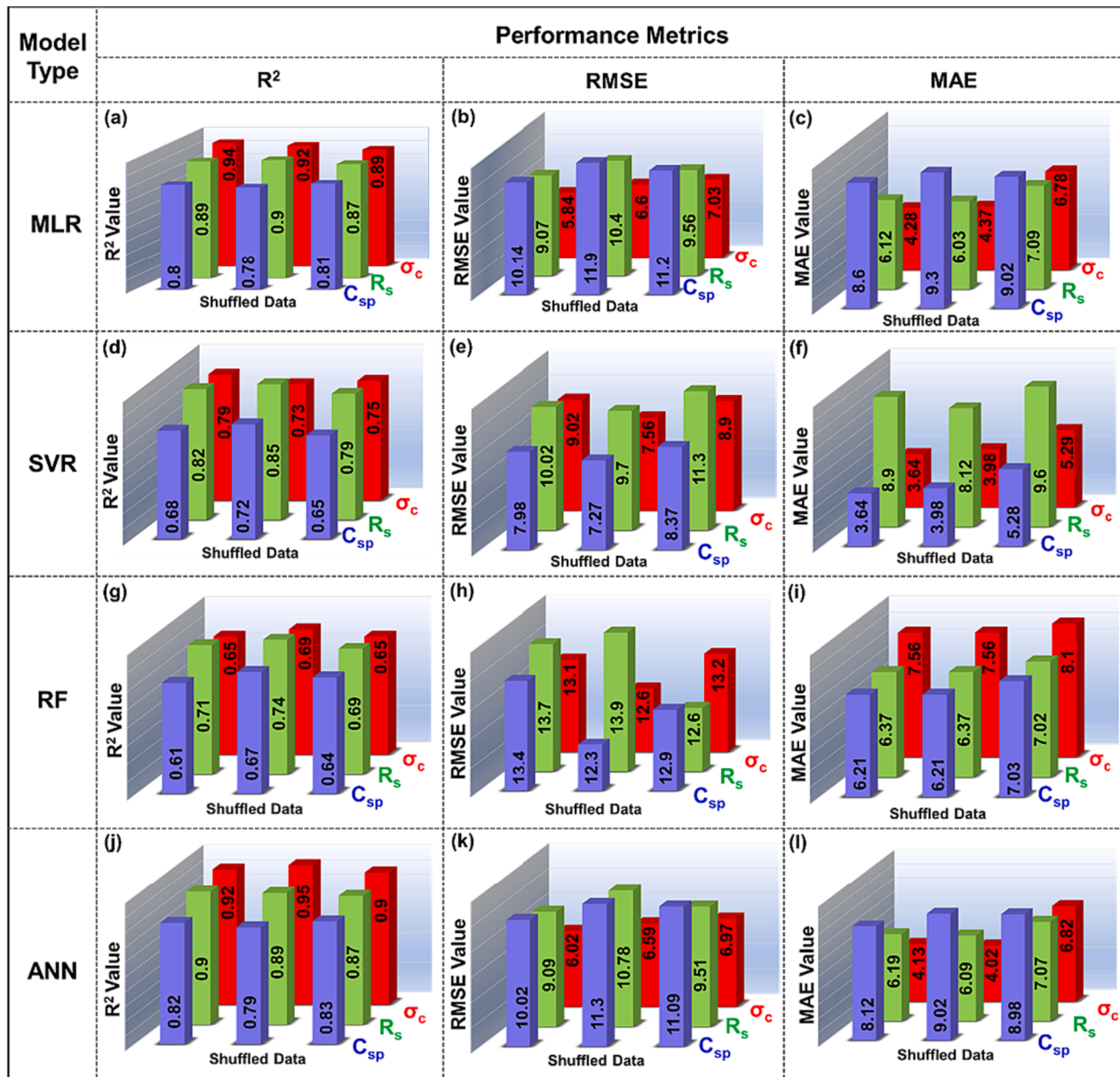


**Fig. 5.** Performance metrics ( $R^2$ , RMSE, MAE) of the four developed ML models. a-c) MLR. d-f) SVR. g-i) RF and j-l) ANN depicting the electrochemical ( $C_{sp}$ ) and electrical performance ( $R_s$  and  $\sigma_c$ ) of MXene/GNPs composites. Among these models ANN shows the highest accuracy for predicting the performance of these composite based supercapacitor electrodes.

while the RMSE value ranges from 7.27 to 8.37 for  $C_{sp}$ , 9.7 to 11.3 for  $R_s$ , 7.56 to 9.02 for  $\sigma_c$  as depicted in Fig. 5d-f respectively. The performance metrics of SVR model were better and achieved as compared to RF model but lower than ANN and MLR respectively. The radial basis function (rbf) as a kernel proved advantageous for learning the linear and non-linear behaviour of output features in SVR model.

Random forest (RF) - The  $R^2$  value in the RF model ranges from 0.61 to 0.67 for  $C_{sp}$ , 0.69 to 0.74 for  $R_s$  and 0.65 to 0.69 for  $\sigma_c$  while RMSE values ranges from 12.3 to 13.4 for  $C_{sp}$ , 12.6 to 13.9 for  $R_s$  and 12.6 to 13.2 for  $\sigma_c$  as mentioned in Fig. 5g-h respectively. This model has achieved the lowest performance metrics as compared to the other three models. This technique uses ensemble learning to train the models, which require a higher volume of data for achieving the higher accuracy and hence RF model did not perform well with the presented case study.

Artificial neural network model (ANN): The  $R^2$  values for ANN range from 0.79 to 0.83 for  $C_{sp}$ , 0.87 to 0.90 for  $R_s$  and 0.90 to 0.95 for  $\sigma_c$  (Fig. 5j). The RMSE values range from 10.02 to 11.3 for  $C_{sp}$ , 9.09 to

10.78 for  $R_s$  and 5.84 to 6.97 for  $\sigma_c$ , which shows the least deviation (Fig. 5k). The minimal increase in RMSE values demonstrates its capability to learn the output feature variations with lesser amount of training data. These achieved metrics of  $R^2$  and RMSE signifies the predictive capability of ANN with the highest accuracy while considering the complex non-linear patterns in the given datasets.

The MAE for all the models is given in Fig. 5c, f, i, l signifying the mean deviation of the predicted values to the real experimental data. ANN significantly outperformed the other three models in the performance metrics. It achieved the highest performance metrics for the predictive values of  $C_{sp}$ ,  $R_s$  and  $\sigma_c$  comprising of one input layer with four neurons (Fig. 6a). The actual output features as obtained from the experiments are plotted against the ANN predicted output values as given in Fig. 6b-d.

#### 2.2.1. ML model performance Comparison

To achieve high predictability, ML models require the sufficient

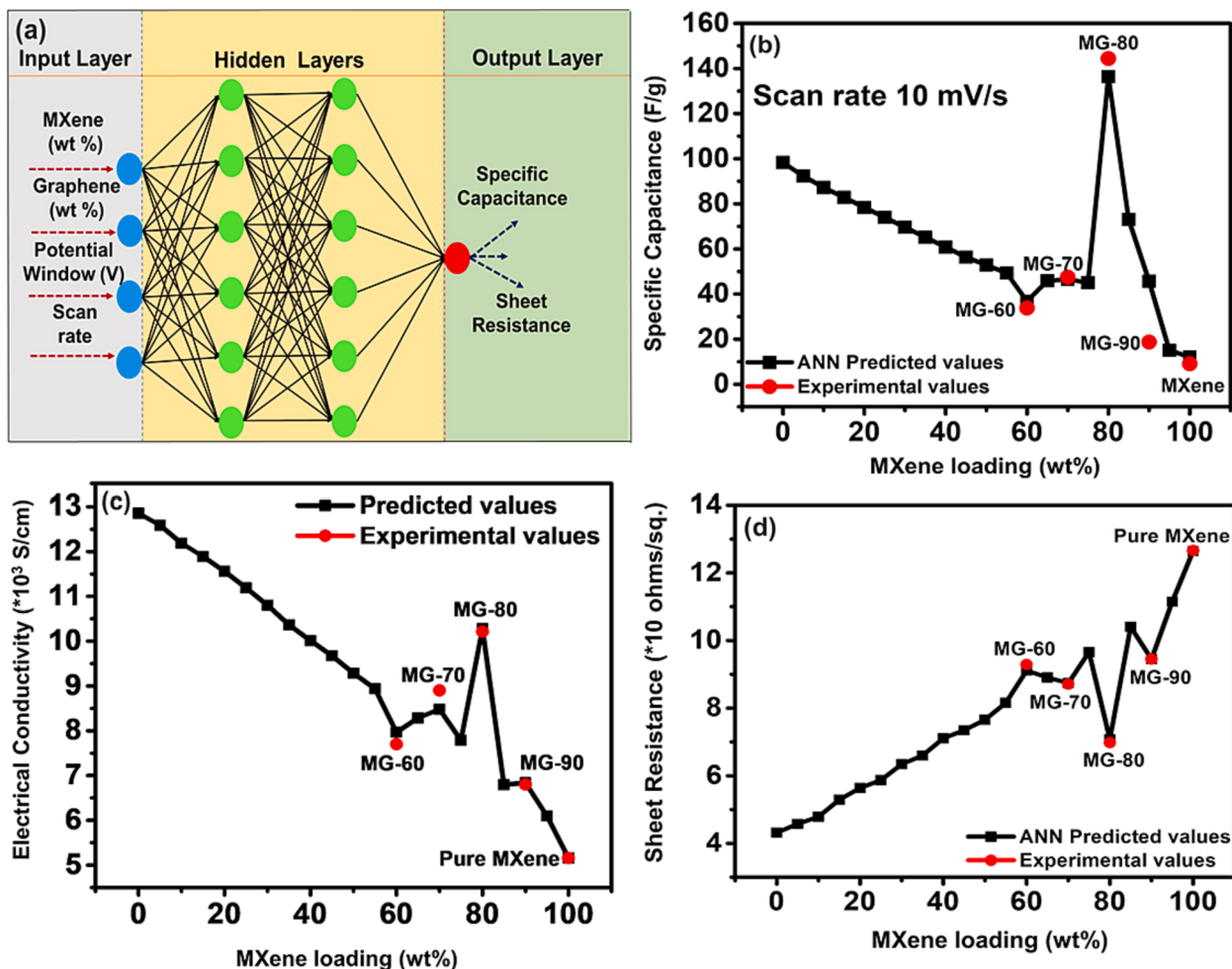


**Fig. 6.** Development of the ANN model predicting the output features for the varying compositions of MXene/GNPs based supercapacitor electrodes. a) Schematic of developed ANN model and Comparison of the experimental and ANN predicted values for b)  $C_{sp}$ , c)  $\sigma_c$ , and d)  $R_s$ .

amount of precise experimental data to train on, whereas this amount is generally limited and difficult to obtain and also increases with the complexity of the interactions between the outcome and the model variables. Among the developed models, MLR had consumed the

minimum computational time for predicting the output features with significantly high accuracy and lower RMSE value range as compared to SVR and RF models as it simplifies the real time data by assuming a linear relationship among the input variables. Multicollinearity can

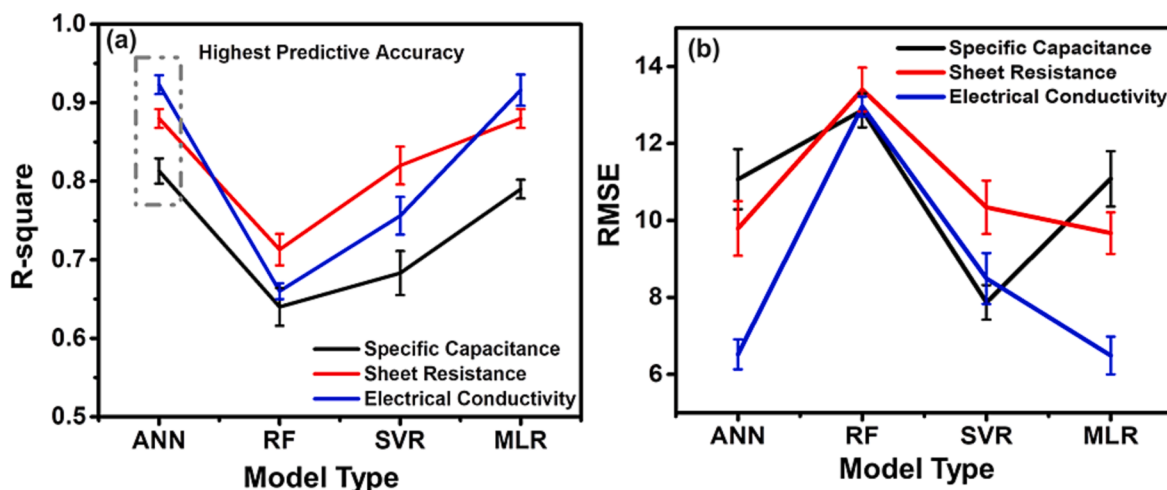


**Fig. 7.** Comparison of the performance metrics of different ML models developed for predicting the electrochemical and electrical performance of MXene/GNPs based supercapacitor electrodes. a) accuracy ( $R^2$ ). b) error (RMSE) value ranges of the developed ML models. The predictive accuracy and error came out to be in the following order of ANN > MLR > SVR > RF.

increase the variance of the coefficient estimates and make the estimates very sensitive to minor changes in the model. Both the SVR and RF model has shown a lower value range of  $R^2$  and higher range of RMSE signifying the large deviation of the predicted data values from the experimental one. These models proved to be more effective in the case of high dimensional spaces where the number of dimensions is greater than the number of samples. In the present case study, the reason behind the low predictive performance of SVR and RF could be its requirement for large sample size and datasets where its maximum likelihood estimates will be more powerful than at ordinary least squares. The SVR model is relatively more based on memory efficient than that of other models because it uses a subset of training points in the decision function (called support vectors). Utilizing the 80 % training data and 20 % testing date, the predictive accuracy and error in terms of  $R^2$  and RMSE of these models came out to be in the following order of ANN > MLR > SVR > RF as shown in Fig. 7a-b.

This developed ANN model for the specific electrochemical performance takes into consideration the correlations between the input features that exist in real-time and influence the supercapacitor electrode behaviour. It showed the profound ability to learn and adapt to the non-linear datasets that resulted in achieving the highest predictive capability of the considered output features. Furthermore, it also established the prediction of the unperformed experimental data with high accuracy metrics.

Both the experimental and ANN computational outcomes exhibited the MG-80 composition with the highest  $C_{sp}$ ,  $\sigma_c$  and lowest  $R_s$  values. Among the various performance indexes of supercapacitors for commercial application, the measurement of the cyclic stability is the next important electrochemical characteristic. It evaluates the quantity of capacitance that is retained after a particular number of charge-discharge cycles eventually measuring the actual service life of the supercapacitors. This ANN model would be beneficial for determining the capacity retention rate of MG-80 electrode for a greater number of cycles (>5000) that can reduce the cost and the time of the experimental testing. Therefore, the capacity retention rate of MG-80 was predicted by utilizing the same ANN model and the datasets were created by the experimental values obtained during the cyclic charging and discharging test upto 5000 cycles.

In order to measure the cyclic stability, the CV and GCD tests of MG-80 were initially carried out. The CV was performed within the same potential window of -0.1 to 0.35 V vs. Ag/AgCl at different scan rates between 5 and 100 mV/s. As depicted in Fig. 8a, the CV response clearly exhibits almost the perfect plateau region demonstrating the double layer as well as pseudo capacitance behaviour. With the presence of pseudo capacitance, the scan rate influences the electrodes and the charge separation and hence the specific capacitance as well [57]. The superior electrochemical performance of MG-80 electrode material was further substantiated by the symmetrical CV curves with oxidation and reduction peaks being maintained even at higher scan rates. The presence of symmetrical triangular plateaus in all the GCD curves are observed at different current densities (Fig. 8b). Initially, there is a sudden drop in the current at the starting point of discharge owing to the internal resistance followed by the linear and slope variation of time dependence of the potential value. The linear variation is the evidence for the presence of double layer capacitance behaviour arising due to the charge separation while slope variation is the result of redox reaction between the electrode and electrolyte interface [58]. With lower values of the current densities, ions of the acidic electrolyte medium ensure more amount of time to infiltrate into the deepest layers of the MXene/GNPs electrode material, thereby efficiently utilizing all the accessible active surface area. While at higher current density values, the ions have lesser time to intercalate into the electrode surface. Therefore, these ions exploit lesser electrochemical active sites available in the outer surface area. Thus, it can be summarized that with the increasing current densities, the capacitive storage capacity and charge-discharge time decrease and vice-versa. As given in Fig. 8c, the capacitance retention

rate of the MG-80 electrode after 5000 cycles was 84.2 %. The curve showed a decrement in the  $C_{sp}$  as steady with the increasing cycles in the MG-80 composite. With the help of ANN model, the capacitance retention rate after 10,000 cycles was predicted to be 63.58 %. With the dataset (refer to Supporting Information in Section 2 as Table S5) as of 5000 cycle test using 80 % training and 20 % testing data, ANN model performance achieved the high predictive accuracy range of ( $R^2$ ) 0.93 to 0.97 with lower RMSE value range of 1.96 to 2.02 (refer to Supporting Information in Section 3 as Fig. S1). These metrics signifies the effectiveness of the ANN model for predicting the capacity retention rate of MG-80 electrode. The achieved  $C_{sp}$  value of 226.6F/g (Fig. 8d) correspond to the as-prepared MG-80 composite, which is superior to the bare MXene and GNPs. The higher  $C_{sp}$  values are achieved at lower scan rate values due to the sufficient time for the electrolyte ions to complete the electrochemical reaction. The decrease in specific capacitance at higher scan rates is attributed to the presence of inner active sites that cannot sustain the redox transitions, which is possibly due to the effects of diffusion of ions within the electrode. The decreasing trend of the capacitance indicates that the parts of the surface of the electrode are inaccessible at high charging/discharging rates [59].

Moreover, the surface area, porosity and pore size distribution are the major contributing parameters having a profound impact on the ion transport in supercapacitors. A large surface area with sufficient inter-layer spacing in the MXene/GNPs composite helps to achieve high capacitance values by facilitating the more active sites for the intercalation and de-intercalation process of ions [60]. The pristine MXene isotherm revealed a similar behaviour as the type III isotherm of the IUPAC classification manual with  $H_3$  type of hysteresis loop in the range of 0.6–1.0P/P<sub>0</sub> implying the behaviour of non-rigid aggregates plate like layered structures having slit shaped pores. In the case of MG-80 composite, the isotherm revealed the type IV classification with  $H_2(b)$  hysteresis loop, suggesting the ordered mesoporous material. The interaction of the GNPs with MXene has increase the surface area capacity while preventing restacking through their combination [61]. With reference to the BET measurements (Fig. 8e and f), the calculated surface area and pore volume of MG-80 increases to 14.25 m<sup>2</sup>/g and 0.014 cc/g as compared to 6.05 m<sup>2</sup>/g and 0.008 cc/g of the bare MXene. This increase in the surface area and pore volume in the composite signifies its enlargement caused by the enveloping of the GNPs into MXene layers. Thus, the overall results show the capability of ANN model, which could be exploited for developing new and efficient electrode in turn minimizing the experimentation time and the cost involved.

To understand the intercalation of GNPs into MXene layers, XPS is utilized to investigate the chemical element states of the bare MXene & MG-80 composite in powder form. The peaks of C1s, O1s and Ti2p can be observed in the survey spectrum shown in the Fig. 9a. The fitting of the XPS spectra revealing Ti<sup>2+</sup> peaks 2P<sub>1/2</sub>, 2P<sub>3/2</sub> and this was fitted into three pairs of peaks 455.2 eV, 460 eV, 463 eV 2P<sub>3/2</sub> and Ti<sup>3+</sup> peaks 461 eV and 455 eV. The Ti 2p scan due to the immediate oxidation on the surface of the MG-80 shown in the Fig. 9b. Overall, three peaks were found in the carbon (1 s) spectrum of MG-80 composite: 285, and 288.6 eV. The 285 eV peak represents the C – C bond. The 288.6 eV peak is attributed to the C – O bond shown in the Fig. 9c [54,62].

The GNPs can interact with the MXene layers through van der Waals forces or  $\pi$ - $\pi$  stacking. These interactions can cause a slight change in the electronic structure of the MXene layers, which can be observed in the XPS spectra. The peaks at 460.2 and 465.4 eV represent Ti – X 2p<sub>1/2</sub> and Ti – X 2p<sub>3/2</sub>, respectively. Three peaks centered at 463.1 and 455 eV were ascribed to Ti – O 2p<sub>1/2</sub> and Ti – O 2p<sub>3/2</sub>, respectively. The C 1 s peak in the survey spectrum of MG80 composite is not shifted significantly as compared to MXene, indicating that the C atoms are not significantly affected by the interaction with the GNPs. According to the XRD and XPS analysis, it is deduced that Mxene/GNPs composite was successfully synthesized.

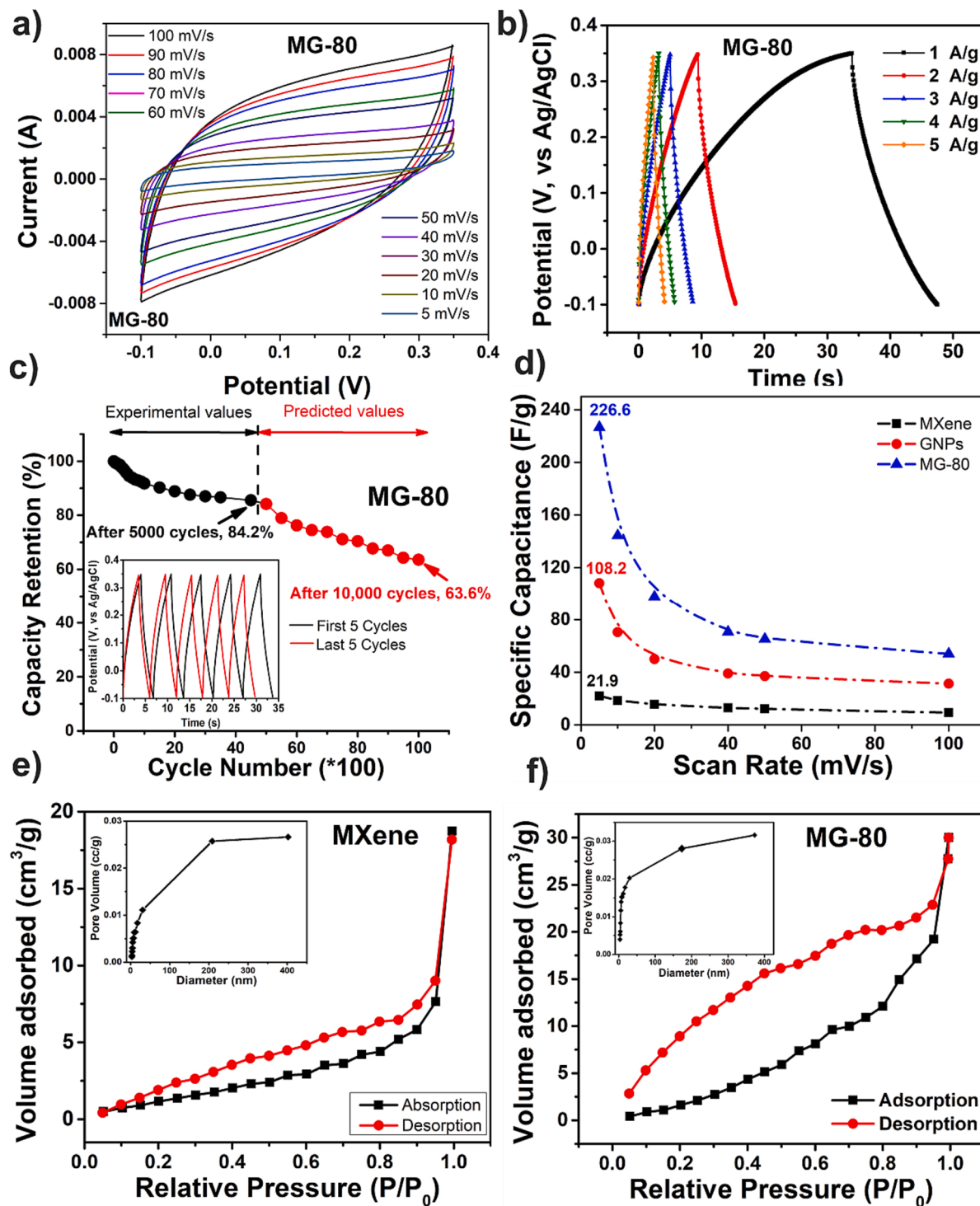


**Fig. 8.** Electrochemical measurements of MG-80 composite in 1 M H<sub>2</sub>SO<sub>4</sub> a) Cyclic voltammetry curves at different scan rates ranging from 5 to 100 mV/s. b) Chronopotentiometry curves at various current densities ranging from 1 to 5 A/g. c) Cyclic stability test performed upto 5000 cycles. d) Comparison of the  $C_{sp}$  values of bare MXene, GNP and MG-80 electrodes calculated at different scan rates calculated. e) N<sub>2</sub> adsorption-desorption isotherm of MXene and f) N<sub>2</sub> adsorption-desorption isotherm of MG-80. Inset plots are their respective pore size distribution. The CV response (a) clearly demonstrate the rise in the peak current values with an increasing scan rate signifying the double layer capacitance behaviour. The presence of symmetrical triangular plateaus in all the GCD curves (b) at different current density values corresponds to the redox nature of the active MG-80 electrode material. The capacitance retention rate of the MG-80 electrode (c) after 5000 cycles was 84.2 %. With the help of ANN model, the capacitance retention rate after 10,000 cycles was predicted to be 63.58 % (c). The achieved  $C_{sp}$  value of 226.6 F/g (d) correspond to the as-prepared MG-80 composite, which is superior to the bare MXene and GNP. The calculated surface area and pore volume of MG-80 increases to 14.25 m<sup>2</sup>/g and 0.014 cc/g (f) as compared to 6.05 m<sup>2</sup>/g and 0.008 cc/g (e) of the bare MXene. This increase in the surface area and pore volume in the composite signifies its enlargement caused by the enveloping of the GNP into MXene layers.

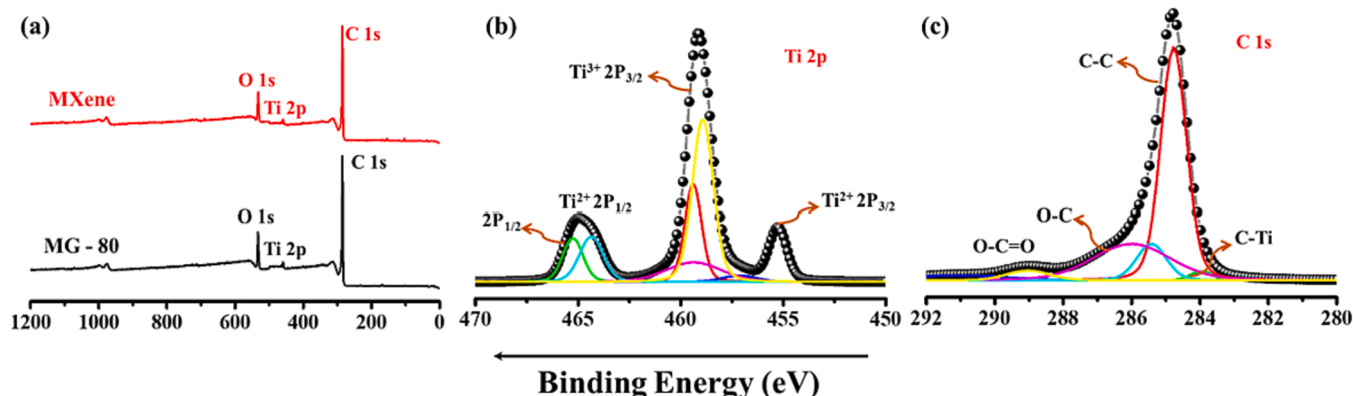


Fig. 9. A) XPS survey spectrum of MXene and MG-80 composite, b)Ti 2p c) C 1 s of MG-80 Composite.

### 3. Conclusion

MXene/GNPs based supercapacitor electrodes were developed in different composition ratios of 10, 20, 30 and 40 wt% of GNPs. XRD, FE-SEM with EDX, HR-TEM and XPS analysis confirmed the effective removal of Al layers from the MAX phase and intercalation of GNPs into  $Ti_3C_2T_x$  sheets. GNPs as fillers helped in non-agglomeration of MXene layers thereby enhancing the electrochemical performance. The data driven ML models were developed and compared using the MLR, SVR, RF and ANN in order to predict the optimum wt.% of GNPs in MXene for achieving the highest electrochemical and electrical properties. The performance metrics of these models follow the ranking of RF < SVR < MLR < ANN respectively. ANN model had outperformed due to its ability to implicitly detect, learn and adapt the complex non-linear relationship between the electrode material, potential operating window, scan rate on the electrochemical and electrical performance of the MXene/GNPs based electrode. Both the experimental and ANN computational results clearly demonstrated the MG-80 electrode composition with the best output features. The synergistic effects of GNPs fillers in the MXene layers helped in achieving the highest  $C_{sp}$  of 226.6 F/g at a scan rate of 5 mV/s. The MG-80 electrode exhibited a capacitance retention rate of 84.2 % after 5000 cycles. Additionally, the developed ANN model was further utilized to predict the retention rate of 63.58 % after 10,000 cycles having an accuracy value range of 0.93–0.97 and error metrics of 1.96–2.02. This work proves the capability of ANN model as a tool for designing the supercapacitor electrodes and the optimum composition of active electrode materials giving higher electrochemical and electrical behaviour.

### 4. Experimental Section

#### a. Synthesis of $Ti_3AlC_2$ MAX powder and $Ti_3C_2T_x$ MXene.

The MAX phase was synthesized by ball-milling TiC (particle size ~2  $\mu$ m), Ti (particle size < 44  $\mu$ m) for 18 h using zirconia balls in plastic jars. The TiC:Ti:Al ratio was 0.9:1.1:1.1. The mixture was heated in an alumina crucible from room temperature (RT) to 1300 °C at 5 °C min<sup>-1</sup> and held for 2 h under flowing Argon. After cooling to room temperature, the block of  $Ti_2AlC$  MAX was crushed via drill-milling and sieved through a 400-mesh sieve (particle size < 38  $\mu$ m).  $Ti_3C_2T_x$  MXene was synthesized from the MAX phase by the step-by-step procedure as reported via mixed-acid method [42,62]. As different from the MILD method, the mixed-acid method protocol comprises of the separate etching and delamination steps. Initially, 3 g of  $Ti_3AlC_2$  MAX powder (particle size < 38  $\mu$ m) was slowly added to 60 mL of etchant containing 12 M HCl (Sigma Aldrich, 37 wt% in H<sub>2</sub>O, 99.9 % trace metals basis) deionized (DI) water, and 48 % HF (in H<sub>2</sub>O, 99.9 % trace metals basis) in a volumetric ratio of 6:3:1, respectively. The polypropylene bottle containing the etchant was immersed in mineral oil at 35 °C and stirred

at 300 rpm for 24 h. The delamination process of the multilayer  $Ti_3C_2T_x$  MXene powder is carried out by mixing it with LiCl (Sigma Aldrich., 99.3 %) in DI water for 24 hrs, resulting in the formation of swelled MXene layers [63,64]. These swelled MXene layered structures can be followed up by either vigorous shaking and stirring for 1 h to convert into few layered MXene [48,52].

#### b. Synthesis of $Ti_3C_2T_x$ MXene/GNPs composite:

The exfoliated  $Ti_3C_2T_x$  MXene is washed several times and dried overnight in vacuum. Finally, GNPs (97 wt% purity, 100–300 nm, Sigma Aldrich) and the partially delaminated MXene are ground physically using a mortar and pestle. The mixed powder is then dispersed in ethanol, sonicated and stirred for 24 h in a cold-water bath followed by 3 h of drying in vacuum to get MXene/GNPs powder. The dried MXene/GNPs powder is used for electrode fabrication (1x1 cm<sup>2</sup>) for the measurements of the electrochemical and electrical properties. The different weight percentages of the prepared composites of MXene and GNPs are specified in Table 2. As a control the synthesized MXene was grounded in the similar manner for the fabrication of the electrode. All the samples where sonicated and underwent uniform experimental procedures for material characterization and electrode preparation.

Note: *The partially delaminated or swelled MXenes may have restricted properties like rheological behaviour and conductivity when compared to their single layers; hence, single-layer MXenes are preferred to enhance the electrochemical and electrical characteristics [45–47].*

c. Materials characterization: X-ray diffraction (XRD) technique of initial MAX phase, MXene and MXene/GNPs based composites were performed using D8 Advanced, Bruker instrument in the 2θ range of 5–70 °C with Cu K $\alpha$  radiation ( $\lambda = 1.5406 \text{ \AA}$ ). The morphology and the elemental composition (in wt. %) were characterized using a FE-SEM instrument (Supra 55 Carl Zeiss, Germany) equipped with EDS (Oxford Liquid Nitrogen free SDD X MAX 50 EDS). HR-TEM of the MXene and MG-80 samples are performed using FEI-TECNAL G2-20 TWIN with LaB6 filament having an operating voltages range of 80 – 200 kV. The powder samples are dispersed in ethanol through sonication. The droplet of the dispersed sample are dropped on the TEM grid and overnight dried at room temperature. The surface area, porosity and pore size distribution were measured by BET and BJH analyses (Quantachrome Autosorb iQ) by studying the adsorption and desorption behaviour of nitrogen gas (77 K) on the samples. XPS analysis is

**Table 2**  
Sample labelling of MXene/GNPs composites in wt.%.

S. No.	Sample Name	MXene wt.%	GNPs wt.%
1	MXene	100	0
2	MG-90	90	10
3	MG-80	80	20
4	MG-70	70	30
5	MG-60	60	40

performed using PHI 5000 versa probe III Scanning XPS Microprobe.

**d. Electrochemical Measurements:** The electrochemical performance of the pristine  $Ti_3C_2T_x$  MXene and MXene/GNPs electrode was examined in a three-electrode cell configuration using 1 M  $H_2SO_4$  aqueous electrolyte. The electrodes were uniformly coated on active area of  $1 \times 1 \text{ cm}^2$  with mass loading of  $1 \text{ mg cm}^{-2}$ . The fabricated electrode (MXene/GNPs/CP), Ag/AgCl, and Pt wire were used as the working, reference, and counter electrodes, respectively. The cyclic voltammetry (CV) measurements were performed within a potential window of  $-0.1 \text{ V}$  to  $0.35 \text{ V}$  vs. Ag/AgCl at different scan rates ranging from 100 to 5 mV/s. The galvanostatic charge–discharge GCD measurements were carried out in a potential window of  $-0.1$  to  $0.35 \text{ V}$  at different current densities of 1, 2, 3, 4 and 5 A/g. From these curves, the  $C_{sp}$  of MXene/GNPs based composites was calculated. The  $C_{sp}$  was calculated through CV and CP curves from Eq. (1) and (2) [65]

$$C_{sp} = \frac{I_{max}}{m(\frac{dv}{dt})} \quad (1)$$

$$C_{sp} = \frac{i \times \Delta t_{\text{discharge}}}{\Delta V \times m} \quad (2)$$

where “ $C_{sp}$ ” is the specific capacitance (in F/g), “ $I$ ” is the current (in A), “ $\Delta t_{\text{discharge}}$ ” is the discharging time (in s), “ $m$ ” is the active mass of the electrode-active material (in g), and “ $\Delta V$ ” is the operating voltage window (in V) of the electrode. The electrochemical impedance spectroscopy (EIS) analysis of the different composite-based electrodes was carried out in a frequency range of  $10^{-1}$  to  $10^5 \text{ Hz}$ . An equivalent RC circuit is utilized to describe the impedance behaviour on the whole frequency range of the supercapacitors as shown in Fig. 10. It is fitted with the Nyquist plot using EC lab software to calculate the equivalent series resistance ( $R_{\text{series}}$ ) and charge transfer resistance ( $R_{CT}$ ).  $R_{\text{series}}$  is obtained by the linear extrapolation of the low frequency part of the Nyquist plot taking the intersection with the real axis. The  $\sigma_c$  and  $R_s$  measurements were done by using the four-point probe method in a semiconductor parameter analyser (Keithley Model 4200 SCS).

**e. Machine Learning Models:** The datasets are constructed with the measured real data of the electrochemical and electrical performance of 10, 20, 30 and 40 wt% of GNPs in MXene, potential window, and scan rate, as input parameters. The models are trained to predict the  $C_{sp}$ ,  $\sigma_c$  and  $R_s$  of different unperformed compositions of MXene and GNPs. Table 3 illustrates the value ranges of the input parameters and output parameters. The detailed theoretical and statistical description of MLR, SVR, RF and ANN is mentioned in Supporting Information in Section 5.

#### Author contribution

MS, SM, ARD, SC, MKN and ANG conceived and designed the work. MS, SM, MM, SP, AA and ANG performed the experiments, characterization and analysis. Finally, MS, SM, ARD, SC, MKN and ANG wrote the manuscript. ANG and MKN supervised the project.

#### CRediT authorship contribution statement

**Mohammed Shariq:** Writing – review & editing, Validation, Methodology, Data curation, Conceptualization. **Sathish Marimuthu:** Writing – original draft, Software, Data curation, Conceptualization. **Amit Rai Dixit:** Writing – original draft, Data curation. **Somnath Chattopadhyaya:** Writing – original draft, Conceptualization. **Saravanan Pandiaraj:** Data curation. **Muthumareeswaran Muthuramamoorthy:** Data curation. **Abdullah N. Alodhyab:** Data curation. **Mohammad Khaja Nazeeruddin:** Writing – review & editing, Validation, Methodology, Data curation, Conceptualization. **Andrews Nirnala Grace:**

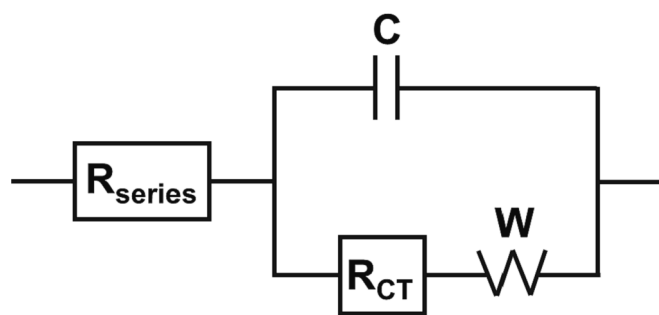


**Fig. 10.** Equivalent circuit representing the supercapacitor cell behaviour on the whole frequency range, where  $R_{\text{series}}$  is the high frequency resistance,  $R_{CT}$  is the resistance of the active material/current collector interface,  $C$  represents the interfacial capacitance at the current collector/active material interface and  $W$  is the diffusion element.

**Table 3**

Range of the Input features for obtaining the Dataset for ML Model Training.

Parameter	Value Range
MXene wt. %	0–100 %
GNPs wt. %	0–100 %
Potential window	$-0.1 \text{ V}$ to $0.35 \text{ V}$
Scan rate	10 mV/s

#### Declaration of competing interest

The authors declare that they have no known competing financial interests or personal relationships that could have appeared to influence the work reported in this paper.

#### Data availability

Data will be made available on request.

#### Acknowledgement

Abdullah Alodhayb extends appreciation to the Deputyship for Research and Innovation, Ministry of Education in Saudi Arabia for funding this research work through project no. (IFKSUOR3–099–6).

The author Sathish Marimuthu thank the DST – PURSE project, India, for funding this research work through the project number [File no. SR/PURSE/2020/34] and Vellore Institute of Technology (VIT), India.

#### Appendix A. Supplementary data

Supplementary data to this article can be found online at <https://doi.org/10.1016/j.cej.2024.149502>.

#### References

- [1] J. Yan, S. Li, B. Lan, Y. Wu, P.S. Lee, Rational design of nanostructured electrode materials toward multifunctional supercapacitors, *Adv. Funct. Mater.* 30 (2020) 1902564, <https://doi.org/10.1002/adfm.201902564>.
- [2] R. Wang, W. Young Jang, W. Zhang, C.h. Venkata Reddy, R.R. Kakarla, C. Li, V. K. Gupta, J. Shim, T.M. Aminabhavi, Emerging two-dimensional (2D) MXene-based nanostructured materials: synthesis strategies, properties, and applications as efficient pseudo-supercapacitors, *Chem. Eng. J.* 472 (2023) 144913, <https://doi.org/10.1016/j.cej.2023.144913>.
- [3] J. Zhang, D. Jiang, L. Liao, L. Cui, R. Zheng, J. Liu,  $Ti_3C_2T_x$  MXene based hybrid electrodes for wearable supercapacitors with varied deformation capabilities, *Chem. Eng. J.* 429 (2022) 132232, <https://doi.org/10.1016/j.cej.2021.132232>.
- [4] A.G. Olabi, Q. Abbas, A. Al Makky, M.A. Abdelkareem, Supercapacitors as next generation energy storage devices: Properties and applications, *Energy* 248 (2022) 123617. 10.1016/j.energy.2022.123617.

- [5] M. Naguib, M.W. Barsoum, Y. Gogotsi, Ten years of progress in the synthesis and development of mxenes, *Adv. Mater.* 33 (2021) 2103393, <https://doi.org/10.1002/adma.202103393>.
- [6] M. Naguib, M. Kurtoglu, V. Presser, J. Lu, J. Niu, M. Heon, L. Hultman, Y. Gogotsi, M.W. Barsoum, Two-dimensional nanocrystals produced by exfoliation of Ti3AlC<sub>2</sub>, *Adv. Mater.* 23 (2011) 4248–4253, <https://doi.org/10.1002/adma.201102306>.
- [7] Z. Haider, S. Fatima, S.A. Zahra, H. Li, S.H.M. Jafri, F. Amin, S. Rizwan, Ag Nanoparticle-decorated V2CTx mxene nanosheets as catalysts for water splitting, *ACS Appl Nano Mater* 6 (2023) 2374–2384, <https://doi.org/10.1021/acsamm.2c04428>.
- [8] M.W. Hakim, S. Fatima, R. Tahir, M.Z. Iqbal, H. Li, S. Rizwan, Ni-intercalated Mo<sub>2</sub>TiC<sub>2</sub>Tx free-standing MXene for excellent gravimetric capacitance prepared via electrostatic self-assembly, *J Energy Storage* 61 (2023) 106662, <https://doi.org/10.1016/j.est.2023.106662>.
- [9] S.A. Zahra, M.M. Mursheed, U. Naeem, T.M. Gesing, S. Rizwan, Cation-assisted self-assembled pillared V2CTx MXene electrodes for efficient energy storage, *Chem. Eng. J.* 474 (2023) 145526, <https://doi.org/10.1016/j.cej.2023.145526>.
- [10] K.R.G. Lim, M. Shekhirev, B.C. Wyatt, B. Anasori, Y. Gogotsi, Z.W. Seh, Fundamentals of mxene synthesis, *Nature Synthesis* 1 (2022) 601–614, <https://doi.org/10.1038/s44160-022-00104-6>.
- [11] S.A. Zahra, B. Anasori, M.Z. Iqbal, F. Ravaux, M. Al Tarawneh, S. Rizwan, Enhanced electrochemical performance of vanadium carbide MXene composites for supercapacitors, *APL Mater.* 10 (2022) 060901, <https://doi.org/10.1063/5.0087457>.
- [12] K. Nasrin, M. Arunkumar, N. Koushik Kumar, V. Sudharshan, S. Rajasekar, D. Mukhilan, M. Arshad, M. Sathish, A rationally designed hetero-assembly of 2D/2D Nitrogen-doped MXene/Graphene via supercritical fluid processing for high energy density supercapacitors, *Chem. Eng. J.* 474 (2023) 145505, <https://doi.org/10.1016/j.cej.2023.145505>.
- [13] S.A. Zahra, E. Ceesay, S. Rizwan, Zirconia-decorated V2CTx MXene electrodes for supercapacitors, *J Energy Storage* 55 (2022) 105721, <https://doi.org/10.1016/j.est.2022.105721>.
- [14] S. Venkateshalu, M. Shariq, N.K. Chaudhari, K. Lee, A.N. Grace, 2D non-carbide MXenes: an emerging material class for energy storage and conversion, *J Mater Chem A Mater* (2022), <https://doi.org/10.1039/D2TA05392F>.
- [15] A. Enaiet Allah, Three-dimensional N-doped mesoporous carbon–MXene hybrid architecture for supercapacitor applications, *RSC Adv.* 13 (2023) 9983–9997, <https://doi.org/10.1039/D2RA06817F>.
- [16] L. Yu, Z. Fan, Y. Shao, Z. Tian, J. Sun, Z. Liu, Versatile N-doped mxene ink for printed electrochemical energy storage application, *Adv. Energy Mater.* 9 (2019) 1901839, <https://doi.org/10.1002/aenm.201901839>.
- [17] X. Gao, X. Du, T.S. Mathis, M. Zhang, X. Wang, J. Shui, Y. Gogotsi, M. Xu, Maximizing ion accessibility in MXene-knotted carbon nanotube composite electrodes for high-rate electrochemical energy storage, *Nat. Commun.* 11 (2020) 6160, <https://doi.org/10.1038/s41467-020-19992-3>.
- [18] A. Zaheer, S.A. Zahra, M.Z. Iqbal, A. Mahmood, S.A. Khan, S. Rizwan, Nickel-adsorbed two-dimensional Nb<sub>2</sub>C MXene for enhanced energy storage applications, *RSC Adv.* 12 (2022) 4624–4634, <https://doi.org/10.1039/D2RA00014H>.
- [19] S.A. Zahra, S. Rizwan, MWCNT-modified MXene as cost-effective efficient bifunctional catalyst for overall water splitting, *RSC Adv.* 12 (2022) 8405–8413, <https://doi.org/10.1039/D2RA00868H>.
- [20] D. Wen, G. Ying, L. Liu, Y. Li, C. Sun, C. Hu, Y. Zhao, Z. Ji, J. Zhang, X. Wang, Direct inkjet printing of flexible MXene/graphene composite films for supercapacitor electrodes, *J. Alloy. Compd.* 900 (2022) 163436, <https://doi.org/10.1016/j.jallcom.2021.163436>.
- [21] D. Wen, G. Ying, L. Liu, C. Sun, Y. Li, Y. Zhao, Z. Ji, Y. Wu, J. Zhang, J. Zhang, X. Wang, Flexible and high-performance mxene/MnO<sub>2</sub> film electrodes fabricated by inkjet printing: toward a new generation supercapacitive application, *Adv. Mater. Interfaces* 8 (2021) 2101453, <https://doi.org/10.1002/admi.202101453>.
- [22] E. Kim, B.-J. Lee, K. Maleski, Y. Chae, Y. Lee, Y. Gogotsi, C.W. Ahn, Microsupercapacitor with a 500 nm gap between MXene/CNT electrodes, *Nano Energy* 81 (2021) 105616, <https://doi.org/10.1016/j.nanoen.2020.105616>.
- [23] K. Gong, K. Zhou, X. Qian, C. Shi, B. Yu, MXene as emerging nanofillers for high-performance polymer composites: a review, *Compos. B Eng.* 217 (2021) 108867, <https://doi.org/10.1016/j.compositesb.2021.108867>.
- [24] J. Luo, E. Matios, H. Wang, X. Tao, W. Li, Interfacial structure design of MXene-based nanomaterials for electrochemical energy storage and conversion, *InfoMat* 2 (2020) 1057–1076, <https://doi.org/10.1002/inf2.12118>.
- [25] X. Zhang, H. Zhang, C. Li, K. Wang, X. Sun, Y. Ma, Recent advances in porous graphene materials for supercapacitor applications, *RSC Adv.* 4 (2014) 45862–45884, <https://doi.org/10.1039/C4RA07869A>.
- [26] S.L. Chiam, H.N. Lim, S.M. Hafiz, A. Pandikumar, N.M. Huang, Electrochemical performance of supercapacitor with stacked copper foils coated with graphene nanoplatelets, *Sci. Rep.* 8 (2018) 3093, <https://doi.org/10.1038/s41598-018-21572-x>.
- [27] Q. Sun, S. Zhu, Z. Shen, Y. Liu, C. Wu, L. Kang, Y. Yang, Molten-salt assisted synthesis of two-dimensional materials and energy storage application, *Mater. Today Chem.* 29 (2023) 101419, <https://doi.org/10.1016/j.mtchem.2023.101419>.
- [28] Q. Chu, H. Lin, M. Ma, S. Chen, Y. Shi, H. He, X. Wang, Cellulose nanofiber/graphene nanoplatelet/mxene nanocomposites for enhanced electromagnetic shielding and high in-plane thermal conductivity, *ACS Appl Nano Mater* 5 (2022) 7217–7227, <https://doi.org/10.1021/acsamm.2c01126>.
- [29] Y. Wang, N. Chen, Y. Liu, X. Zhou, B. Pu, Y. Qing, M. Zhang, X. Jiang, J. Huang, Q. Tang, B. Zhou, W. Yang, MXene/graphdiyne nanotube composite films for free-standing and flexible solid-state supercapacitor, *Chem. Eng. J.* 450 (2022) 138398, <https://doi.org/10.1016/j.cej.2022.138398>.
- [30] C. Gao, X. Min, M. Fang, T. Tao, X. Zheng, Y. Liu, X. Wu, Z. Huang, Innovative materials science via machine learning, *Adv. Funct. Mater.* 32 (2022) 2108044, <https://doi.org/10.1002/adfm.202108044>.
- [31] C. Bilodeau, A. Kazakov, S. Mukhopadhyay, J. Emerson, T. Kalantar, C. Muzny, K. Jensen, Machine learning for predicting the viscosity of binary liquid mixtures, *Chem. Eng. J.* 464 (2023) 142454, <https://doi.org/10.1016/j.cej.2023.142454>.
- [32] T. Yasuda, S. Ookawara, S. Yoshikawa, H. Matsumoto, Materials processing model-driven discovery framework for porous materials using machine learning and genetic algorithm a focus on optimization of permeability and filtration efficiency, *Chem. Eng. J.* 453 (2023) 139540, <https://doi.org/10.1016/j.cej.2022.139540>.
- [33] M. Zhou, A. Vassallo, J. Wu, Data-driven approach to understanding the in-operando performance of heteroatom-doped carbon electrodes, *ACS Appl Energy Mater* 3 (2020) 5993–6000, <https://doi.org/10.1021/acsam.0c01059>.
- [34] H. Su, S. Lin, S. Deng, C. Lian, Y. Shang, H. Liu, Predicting the capacitance of carbon-based electric double layer capacitors by machine learning, *Nanoscale Adv* 1 (2019) 2162–2166, <https://doi.org/10.1039/C9NA00105K>.
- [35] S. Nanda, S. Ghosh, T. Thomas, Machine learning aided cyclic stability prediction for supercapacitors, *J. Power Sources* 546 (2022) 231975, <https://doi.org/10.1016/j.jpowsour.2022.231975>.
- [36] L. Wang, S. Gao, W. Li, A. Zhu, H. Li, C. Zhao, H. Zhang, W.-H. Wang, W. Wang, Machine learning assisted screening of MXenes pseudocapacitive materials, *J. Power Sources* 564 (2023) 232834, <https://doi.org/10.1016/j.jpowsour.2023.232834>.
- [37] S. Zhu, J. Li, L. Ma, C. He, E. Liu, F. He, C. Shi, N. Zhao, Artificial neural network enabled capacitance prediction for carbon-based supercapacitors, *Mater. Lett.* 233 (2018) 294–297, <https://doi.org/10.1016/j.matlet.2018.09.028>.
- [38] M. Rahimi, M.H. Abbaspour-Fard, A. Rohani, Synergetic effect of N/O functional groups and microstructures of activated carbon on supercapacitor performance by machine learning, *J. Power Sources* 521 (2022) 230968, <https://doi.org/10.1016/j.jpowsour.2021.230968>.
- [39] C. Qian, K. Sun, W. Bao, Recent advance on machine learning of MXenes for energy storage and conversion, *Int. J. Energy Res.* 46 (2022) 21511–21522, <https://doi.org/10.1002/er.7833>.
- [40] J. Zhu, Y. Wang, Y. Huang, R. Bhushan Gopaluni, Y. Cao, M. Heere, M. J. Mühlbauer, L. Mereacre, H. Dai, X. Liu, A. Senyshyn, X. Wei, M. Knapp, H. Ehrenberg, Data-driven capacity estimation of commercial lithium-ion batteries from voltage relaxation, *Nat. Commun.* 13 (2022) 2261, <https://doi.org/10.1038/s41467-022-29837-w>.
- [41] Y. Zhang, Q. Tang, Y. Zhang, J. Wang, U. Stimming, A.A. Lee, Identifying degradation patterns of lithium ion batteries from impedance spectroscopy using machine learning, *Nat. Commun.* 11 (2020) 1706, <https://doi.org/10.1038/s41467-020-15235-7>.
- [42] M. Alhabeb, K. Maleski, B. Anasori, P. Lelyukh, L. Clark, S. Sin, Y. Gogotsi, Guidelines for synthesis and processing of two-dimensional titanium carbide (Ti3C2Tx MXene), *Chem. Mater.* 29 (2017) 7633–7644, <https://doi.org/10.1021/acs.chemmater.7b02847>.
- [43] K. Hou, Y. Yang, H. Zhou, X. Chen, S. Ge, Enhanced yield of large-sized Ti3C2Tx mxene polymers nanosheets via cyclic ultrasonic-centrifugal separation, *Polymers (basel)* 15 (2023), <https://doi.org/10.3390/polym15061330>.
- [44] Q. Zhang, R. Fan, W. Cheng, P. Ji, J. Sheng, Q. Liao, H. Lai, X. Fu, C. Zhang, H. Li, Synthesis of large-area mxenes with high yields through power-focused delamination utilizing vortex kinetic energy, *Adv. Sci.* 9 (2022) 2202748, <https://doi.org/10.1002/advs.202202748>.
- [45] K.A.S. Usman, S. Qin, L.C. Henderson, J. Zhang, D.Y. Hegh, J.M. Razal, Ti3C2Tx MXene: from dispersions to multifunctional architectures for diverse applications, *Mater. Horiz.* 8 (2021) 2886–2912, <https://doi.org/10.1039/DMH00968K>.
- [46] B. Akuzum, K. Maleski, B. Anasori, P. Lelyukh, N.J. Alvarez, E.C. Kumbar, Y. Gogotsi, Rheological characteristics of 2D titanium carbide (MXene) dispersions: a guide for processing mxenes, *ACS Nano* 12 (2018) 2685–2694, <https://doi.org/10.1021/acsnano.7b08889>.
- [47] S. Abdolhosseiniزاده, X. Jiang, H. Zhang, J. Qiu, C. (John) Zhang, Perspectives on solution processing of two-dimensional MXenes, *Mater. Today* 48 (2021) 214–240, <https://doi.org/10.1016/j.mattod.2021.02.010>.
- [48] A. Thakur, N. Chandran B.S., K. Davidson, A. Bedford, H. Fang, Y. Im, V. Kanduri, B.C. Wyatt, S.K. Nemani, V. Polikutova, R. Kumar, Z. Fakhraei, B. Anasori, Step-by-Step Guide for Synthesis and Delamination of Ti3C2Tx MXene, *Small Methods* 7 (2023). <https://doi.org/10.1002/smtd.202300030>.
- [49] D. Bhattacharjya, I.-Y. Jeon, H.-Y. Park, T. Panja, J.-B. Baek, J.-S. Yu, Graphene nanoplatelets with selectively functionalized edges as electrode material for electrochemical energy storage, *Langmuir* 31 (2015) 5676–5683, <https://doi.org/10.1021/acs.langmuir.5b0195>.
- [50] T. Zhou, C. Wu, Y. Wang, A.P. Tomsia, M. Li, E. Saiz, S. Fang, R.H. Baughman, L. Jiang, Q. Cheng, Super-tough MXene-functionalized graphene sheets, *Nat. Commun.* 11 (2020) 2077, <https://doi.org/10.1038/s41467-020-15991-6>.
- [51] J. Yan, C.E. Ren, K. Maleski, C.B. Hatter, B. Anasori, P. Urbankowski, A. Sarycheva, Y. Gogotsi, Flexible mxene/graphene films for ultrafast supercapacitors with outstanding volumetric capacitance, *Adv. Funct. Mater.* 27 (2017) 1701264, <https://doi.org/10.1002/adfm.201701264>.
- [52] M. Shekhirev, J. Busa, C.E. Shuck, A. Torres, S. Bagheri, A. Sinitskii, Y. Gogotsi, Ultralarge flakes of Ti3C2Tx mxene via soft delamination, *ACS Nano* 16 (2022) 13695–13703, <https://doi.org/10.1021/acsnano.2c04506>.
- [53] S.S. Shankar, R.M. Shereema, R.B. Rakhi, Electrochemical determination of adrenaline using mxene/graphite composite paste electrodes, *ACS Appl. Mater. Interfaces* 10 (2018) 43343–43351, <https://doi.org/10.1021/acsami.8b11741>.
- [54] X. Yang, Q. Wang, K. Zhu, K. Ye, G. Wang, D. Cao, J. Yan, 3D porous oxidation-resistant mxene/graphene architectures induced by in situ zinc template toward

- high-performance supercapacitors, *Adv. Funct. Mater.* 31 (2021) 2101087, <https://doi.org/10.1002/adfm.202101087>.
- [55] B. Rani, N.K. Sahu, Electrochemical properties of CoFe<sub>2</sub>O<sub>4</sub> nanoparticles and its rGO composite for supercapacitor, *Diam. Relat. Mater.* 108 (2020) 107978, <https://doi.org/10.1016/j.diamond.2020.107978>.
- [56] F. Sundfors, J. Bobacka, EIS study of the redox reaction of Fe(CN)<sub>6</sub>3-/4- at poly(3,4-ethylenedioxythiophene) electrodes: influence of dc potential and cOx:Red ratio, *J. Electroanal. Chem.* 572 (2004) 309–316, <https://doi.org/10.1016/j.jelechem.2003.12.013>.
- [57] K. Li, X. Wang, X. Wang, M. Liang, V. Nicolosi, Y. Xu, Y. Gogotsi, All-pseudocapacitive asymmetric MXene-carbon-conducting polymer supercapacitors, *Nano Energy* 75 (2020) 104971, <https://doi.org/10.1016/j.nanoen.2020.104971>.
- [58] A.N. Grace, R. Ramachandran, M. Vinoba, S.Y. Choi, D.H. Chu, Y. Yoon, S.C. Nam, S.K. Jeong, Facile synthesis and electrochemical properties of Co<sub>3</sub>S<sub>4</sub>-nitrogen-doped graphene nanocomposites for supercapacitor applications, *Electroanalysis* 26 (2014) 199–208, <https://doi.org/10.1002/elan.201300262>.
- [59] M.R. Lukatskaya, S. Kota, Z. Lin, M.-Q. Zhao, N. Shpigel, M.D. Levi, J. Halim, P.-L. Taberna, M.W. Barsoum, P. Simon, Y. Gogotsi, Ultra-high-rate pseudocapacitive energy storage in two-dimensional transition metal carbides, *Nat. Energy* 2 (2017) 17105, <https://doi.org/10.1038/nenergy.2017.105>.
- [60] J. Yang, W. Bao, P. Jaumaux, S. Zhang, C. Wang, G. Wang, MXene-based composites: synthesis and applications in rechargeable batteries and supercapacitors, *Adv. Mater. Interfaces* 6 (2019) 1802004, <https://doi.org/10.1002/admi.201802004>.
- [61] G.A. Tompsett, L. Krogh, D.W. Griffin, W.C. Conner, Hysteresis and scanning behavior of mesoporous molecular sieves, *Langmuir* 21 (2005) 8214–8225, <https://doi.org/10.1021/la050068y>.
- [62] S. Shi, R. Zhong, L. Li, C. Wan, C. Wu, Ultrasound-assisted synthesis of graphene@MXene hybrid: a novel and promising material for electrochemical sensing, *Ultrason. Sonochem.* 90 (2022) 106208, <https://doi.org/10.1016/j.ulsonch.2022.106208>.
- [63] N. Kurra, S. Uzun, G. Valuorouthu, Y. Gogotsi, Mapping (pseudo)capacitive charge storage dynamics in titanium carbide mxene electrodes in aqueous electrolytes using 3d bode analysis, *Energy Storage Mater.* 39 (2021) 347–353, <https://doi.org/10.1016/j.ensm.2021.04.037>.
- [64] M. Anayee, N. Kurra, M. Alhabeb, M. Seredysh, M.N. Hedhili, A.-H. Emwas, H. N. Alshareef, B. Anasori, Y. Gogotsi, Role of acid mixtures etching on the surface chemistry and sodium ion storage in Ti<sub>3</sub>C<sub>2</sub>T<sub>x</sub> MXene, *Chem. Commun.* 56 (2020) 6090–6093, <https://doi.org/10.1039/D0CC01042A>.
- [65] S. Venkateshalu, J. Cherusseri, M. Karnan, K.S. Kumar, P. Kollu, M. Sathish, J. Thomas, S.K. Jeong, A.N. Grace, New method for the synthesis of 2D vanadium nitride (mxene) and its application as a supercapacitor electrode, *ACS Omega* 5 (2020) 17983–17992, <https://doi.org/10.1021/acsomega.0c01215>.